Self-Recoverable Mechanically Induced Instant Luminescence from Cr 3+ -Doped LiGa 5 O 8

Puxian Xiong, Bolong Huang, Dengfeng Peng, Bruno Viana, Mingying Peng, Zhijun Ma

Self-Recoverable Mechanically Induced Instant Luminescence from Cr^{3+}-Doped $LiGa_5O_8$

Puxian Xiong, Bolong Huang, Dengfeng Peng, Bruno Viana, Mingying Peng, Zhijun Ma
First published: 03 March 2021
https://doi.org/10.1002/adfm.202010685

School of Physics and Optoelectronic, The State Key Laboratory of Luminescent Materials and Devices, and Guangdong Provincial Key Laboratory of Fiber Laser Materials and Applied Techniques South China University of Technology, Guangzhou 510640, China.
Department of Applied Biology and Chemical Technology, The Hong Kong Polytechnic University, Hong Hum, Kowloon, Hong Kong SAR, China
College of Physics and Optoelectronic Engineering, Shenzhen University, Shenzhen 518060, China
PSL Research University Chimie ParisTech, IRCP, CNRS, Paris 75005, France
The China-Germany Research Center for Photonic Materials and Device, The State Key Laboratory of Luminescent Materials and Devices, and Guangdong Provincial Key Laboratory of Fiber Laser Materials and Applied Techniques, The School of Materials Science and Engineering, South China University of Technology, Guangzhou 510641, China.

* Corresponding author.
E-mail: pengmingying@scut.edu.cn (M.Y. Peng)； zhijma@scut.edu.cn (Z. J. Ma)

Abstract:

Mechanoluminescence (ML) featuring photon emission under external mechanical stimuli has been widely investigated due to its potential applications in various fields such as display, pressure monitoring and energy harvesting. However, except for doped ZnS, all the existing ML phosphors require light pre-irradiation to power ML, which hinders practical applications. Meanwhile, except Mn^{2+} and Cu^{+}, no other transition metal cation has been established as effective activator for ML phosphors. In the present paper, for the first time, one report the self-recoverable deep-red-to-near-infrared ML in Cr^{3+} doped $LiGa_5O_8$ phosphor without any light pre-irradiation. Furthermore the mechanoluminescence intensity of this phosphor can be fully restored after each mechanical loading cycle. One further demonstrate that by codoping

the compounds with Al^{3+} cations in order to tune traps redistribution, the ML performance of the phosphor can be further optimized. Then a possible mechanism for ML in Cr^{3+} doped $LiGa_5O_8$ phosphor is proposed. Theoretical calculations reveal the significant role of Cr dopants in the modulation of the local electronic environments for achieving ML. Owing to the induced inter-electronic-levels and shallow electron traps distribution, electron recombination efficiency is enhanced both through tunneling effect and energy transfer toward dopant levels. Such ML can penetrate through a 2 mm-thick pork slice including skin, fat and lean, making this material promising for wide range of *in-vivo* applications such as optical imaging of intracorporal stress/strain distribution and dynamics. The present work offers an example of material suitable in new wavelengths range thank to new ML activator, fulfilling a research gap in ML research field and this work is expected to promote further advancement of ML materials both fundamentally and practically.

Keywords: self-recoverable mechanoluminescence, biostress visualization, trivalent Cr, $LiGa_5O_8$

1. Introduction

Mechanoluminescence (ML) represents an amazing process of materials photon emission under mechanical stimuli such as grinding, compressing, fracturing or stretching.[1-6] Due to the instantaneous and in situ characteristics of ML, mechanical induced luminescent materials have shown huge potentials in various fields such as mechanical sensing,[7] magnetic-optics coupling,[8] visualized sensing,[9] dynamic pressure mapping[10] and organic piezo-display devices.[2, 11] In particular, ML materials possess unique advantages in mechanical sensing, because they can provide in-situ, real-time and multi-dimensional stress/strain sensing.[11-13] Generally, most ML materials required to be pre-irradiated before applications typically by a high energy ultraviolet light. Once the pre-stored charges are released (to generate ML emission), they have to be irradiated again and again for further use. Although in some applications, the ML materials can be coated on the surface of the target object,[14] so that one can pre-irradiate them if necessary directly after each load cycle. Such in-need pre-irradiation strategy fails to work in some other applications wherein ML materials are buried inside and

are unable to receive light irradiation. Especially, the shallow tissue penetration depth and possible tissue damage caused by the high-energy UV light (for powering ML materials) will also limit the applications of current ML materials needing light pre-irradiation for in vivo biomedical applications. Thus, developing novel ML materials which can penetrate tissues featuring self-recoverable ML emissions is urgently required and this work is the first step toward this aim. In the future, dispersible nanomaterials stable in biological medium should be developed but this is not the scope of the present paper focus on the proof of concept.

Till now, many ML materials have been reported, wherein piezoelectric hosts such as $LiNbO_3$, (Ca/Ba)OZnS and ZnS play dominant role.[15-20] Generally, most ML phosphors are trap dependent.[21, 22] Following this idea, ML materials can be divided into two categories: phosphors which need light pre-irradiation (non-self-recoverable) and phosphors which do not need light pre-irradiation for ML (self-recoverable).[3] At present, self-recoverable ML was only discovered in Mn^{2+}/Cu^{+} doped ZnS phosphor. In 2013, Jeong et al. found that ML from the ZnS:Cu^{+} -polymer composite film demonstrates ML with reproducible intensity over 100,000 cycles of repeated stretching.[23] Afterwards, in 2015, Wang et al. reported that composite film dispersed with ZnS:Mn^{2+} phosphor can show stable ML intensity in over 10,000 cycles of repeated compression tests [10]. The authors attribute the recoverability of intense ML to the fact that both stretching and releasing processes can induce local electrical field that excites ZnS:Mn^{2+} which relax through ML.[10] However, as for the self-recoverable ML phenomenon, no convincing mechanism has been proposed.[23] For this regard, Kim et al. have found that the triboelectricity-induced luminescence may be more likely to contribute to the mechanically driven luminescence in ZnS.[24] Afterwards, Zhu et al. fabricated a composite with ZnS:Cu/poly (methyl methacrylate) as luminescent layer. They also certified that ZnS type phosphors present mechanical induced electroluminescence.[9] Considering the ideas from Wang et al. and the outstanding self-recoverable ML from doped ZnS materials, which hardly can be realized by other non-piezoelectrical ML materials, one can consider doped ZnS as a piezoelectricity-induced electroluminescent material. However, this model cannot explain the ML properties of materials such as $SrAl_2O_4$:Eu^{2+} by weak mechanical stimuli, in which only too weak piezoelectric field can be formed to impact and excite Eu^{2+}. Others researchers

propose that the piezoelectricity-induced de-trapping model may also be responsible for the origin of ML.[2, 15] This model has been used towards many ML phosphors. However, no self-recoverable ML phosphor based on this kind of model has been discovered until now.[25] In addition, the emission centers of existing ML phosphors are mostly based on lanthanide cations such as Nd^{3+}, Sm^{3+}, Tm^{3+} and Pr^{3+}.[26-28] To the best of our knowledge, except for Cu^{+} and Mn^{2+}, no other transition metal cation has been proved to be active as ML emission center.

Compared to Mn^{2+}/Cu^{+} doped ZnS phosphors, Cr^{3+} activated deep-red persistent luminescence gallate ($LiGa_5O_8$ for instance) materials have drawn much attention and shown potential applications in bioimaging [ ], however, no ML from Cr^{3+} ions has ever been reported. Here, for the first time, we report the self-recoverable (free of light pre-irradiation) deep-red-to-near-infrared ML in Cr^{3+} doped $LiGa_5O_8$ phosphor. Cr^{3+} is substituted into the 6-coordiated Ga^{3+} site (as well stabilized in the octahedral gallium sites) to further generate ML peaking at 716 nm from its $^2E \rightarrow {}^4A_2$ spin forbidden transition.[29, 30] As we have found that deeper traps (in the bandgap with energy >1.06 eV) may be important to ML, we enhance the trap distribution by codoping with Al^{3+} ions. Moreover, the recovery of the self-recoverable ML can be achieved after each cycle, without any assistance from new light excitation. Here, based on these results, a possible mechanism based on mechanical-induced trap recharging is proposed to be responsible for the origin of the self-recoverable ML in Cr^{3+} doped $LiGa_5O_8$. DFT calculations unravel the formation of local piezoelectrical field induced by the incorporation of Cr in $LiGa_5O_8$ host, which enhances electronic transfers but also promotes energy conversion. Finally, we demonstrate that such ML can penetrate deeply animal soft tissue to offer potential biomedical applications.

2 Material and methods

2.1 Synthesis of the $LiGa_5O_8:Cr^{3+}$ and $LiGa_{5-x}Al_x O_8:Cr^{3+}$ powders

All $LiGa_5O_8:Cr^{3+}$ and $LiGa_5O_8:Cr^{3+}$, Al^{3+} (or $LiGa_{5-x}Al_x O_8:Cr^{3+}$) powders were synthesized by high-temperature solid state reaction[31]. High purity Li_2CO_3 (99.99%, Aladdin), Ga_2O_3 (99.99%, Aladdin), Al_2O_3 (99.99%, Aladdin) and Cr_2O_3 (99.99%, Aladdin) were weighed

according to the chemical composition $LiGa_{5(1-x)}O_8:5xCr^{3+}$ (x=0.04%, 0.08%, 0.12%, 0.16%, 0.20% and 0.24%) and $LiGa_{4.994(1-y)}O_8:0.6\%Cr^{3+}$, $4.994yAl^{3+}$ (y= 0, 0.02%, 0.04%, 0.06%, 0.08% and 0.10%) powders were ground in an agate mortar. Then, the samples were sintered with an air flow initially at 800 ºC for 2 h and consequently at 1400 ºC for 4 h. After sintering, the samples were slowly cooled down to room temperature in the furnace, and were ground again for subsequent characterizations.

2.2 Characterizations

The crystalline phases of $LiGa_{5(1-x)}O_8:5xCr^{3+}$ (x=0.04%, 0.08%, 0.12%, 0.16%, 0.20% and 0.24%) and $LiGa_{4.994(1-y)}O_8:0.6\%Cr^{3+}$, $4.994yAl^{3+}$ (y= 0, 0.02%, 0.04%, 0.06%, 0.08% and 0.10%) were characterized using an X-ray diffractometer (Rigaku D/max-IIIA) with Cu-Kα1 radiation (1.5405 Å; cathode voltage, 40 kV; current, 40 mA) as X-ray radiation source and swept in the 2θ range of 10°-90° at room temperature. Raw XRD data were further analyzed using Rietveld refinement method (FullProf software package) to confirm the formation of the target phase, and the crystal structure of $LiGa_5O_8$ was redrawn according to $LiGa_5O_8$ PDF number 38-1371. Diffuse reflectance (DR) spectra were obtained with an Agilent Cary 60 ultraviolet-visible spectrometer over the range 200-1000 nm using $BaSO_4$ powder as a standard reference. Morphological and elemental analysis were characterized with a Hitachi S-3700 scanning electron microscope (SEM) equipped with an energy-dispersive X-ray spectrometer (EDS) at a working voltage of 15.0 kV. Static photoluminescence excitation (PLE), emission (PL) and persistent luminescence (PersL) spectra were recorded using an Edinburgh FLS920 fluorescence spectrophotometer equipped with a 450 W Xe lamp source. For thermoluminescence (TL) measurements, the samples were pre-irradiated by a 15 W, 254 nm lamp. TL glow curves were recorded using an FJ427A1 thermoluminescent dosimeter (CNNC Beijing Nuclear Instruments Factory) in the range of 320~620 K at a heating rate of 2 K/s. To evaluate the ML properties of samples, composite pellets (diameter 25 mm; thickness ~5 mm) were prepared by mixing the ML powders with an optical epoxy resin (ZM DIY) at the mass ratio of 1:4. The epoxy resin and the powders were mixed by magnetic stirring for 20 minutes to favor the dispersing homogeneity of powders. The ML spectra were recorded by a photo-counting system consisting of an (QE65pro, Ocean Optics) optical spectrophotometer. A borosilicate glass rod was used to quickly slide on the surface of the

pellet while the TML (ML excited by friction) signals were recorded by the photo-counting system at an integration time of 2 s. All the images were recorded by a Canon EOS 700D digital camera (ISO: 3200, AV mode, EFS 18–55 mm).

2.3 Calculation Setup

All the calculations have been carried out through the density functional theory (DFT) within the CASTEP packages regarding the electronic structures and energy cost of doping[32, 33]. For all the calculations, we choose the generalized gradient approximation (GGA) and Perdew-Burke-Ernzerhof (PBE) to reveal the exchange-correlation energy[34-36]. We select the 410 eV cut off energy within the ultrasoft pseudopotential scheme for all geometry optimizations[37]. The Broyden-Fletcher-Goldfarb-Shannon (BFGS) algorithm is applied to the k-point mesh to achieve energy minimizations[38, 39]. For all geometry optimizations, we set the convergence criteria for the geometry optimizations as below: the Hellmann-Feynman forces should not exceed 0.001 eV per angstrom and the total energy should be less than 5×10^{-5} eV per atom. The doping of the Cr atom has been placed in the position of Ga site to align with the experimental observations and the doping concentration is 5% for all the theoretical calculations.

3 Results and discussion

3.1 Crystalline structure and micromorphology of $LiGa_5O_8:Cr^{3+}$

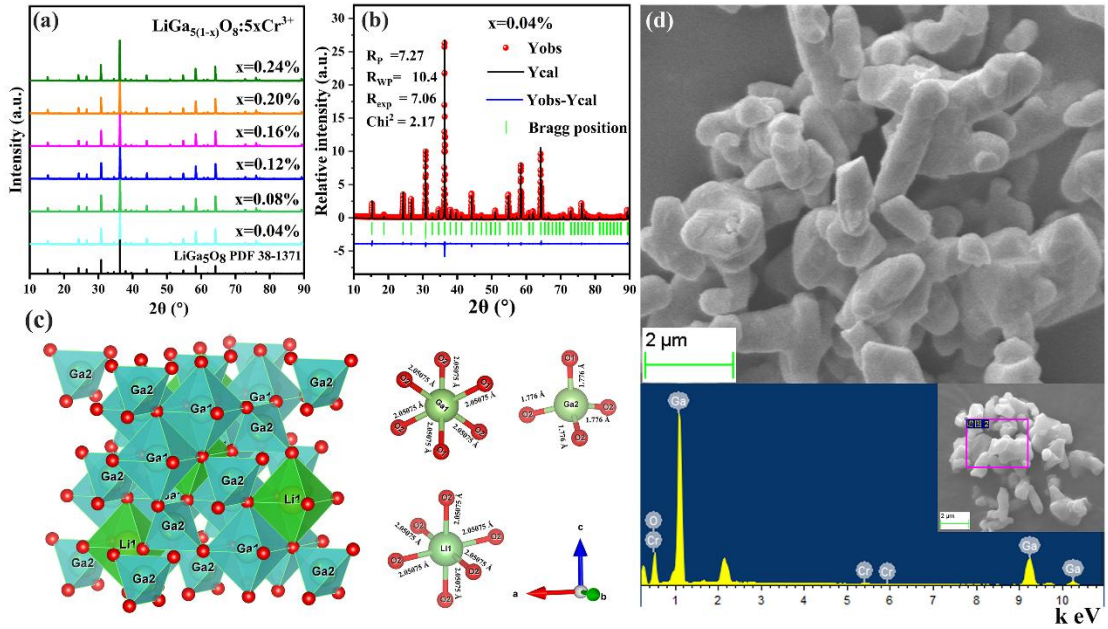

Fig. 1 Crystalline structure and micromorphology of $LiGa_5O_8:Cr^{3+}$. (a) XRD patterns of $LiGa_{5(1-x)}O_8:5xCr^{3+}$ (x= 0.04%, 0.08%, 0.12%, 0.16%, 0.20% and 0.24%) and standard card of $LiGa_5O_8$ (PDF 38-1371). (b) XRD pattern (red ○, Y_{obs}) of the sample x=0.04%, Rietveld refining results (black−, Y_{cal}), Bragg reflections (green |, Bragg position) and the profile difference between experimental and calculated values (blue −, Y_{obs}-Y_{cal}). (c) Scheme for the crystalline structure of $LiGa_5O_8$ redrawn on the basis of PDF 38-1171 using VESTA program. (d) SEM image (upside) and EDS pattern (downside, the unlabeled peaks are from Au element brought by the sputtering process before test) of sample x=0.04%.

XRD patterns of $LiGa_{5(1-x)}O_8:5xCr^{3+}$ (x=0.04%, 0.08%, 0.12%, 0.16%, 0.20% and 0.24%) are depicted in Fig. 1(a). Compared to the reference spectrum of $LiGa_5O_8$, it can be confirmed that cubic $LiGa_5O_8$ (PDF 38-1371) dominates the crystalline phase in all doped samples. This means that all Cr^{3+} ions are well incorporated into the $LiGa_5O_8$ lattice. To determine the actual crystalline structure of the obtained samples, Rietveld refinement is performed on sample x=0.04%, as presented in Fig. 1(b). The refinement starts with the powder diffraction data of $LiGa_5O_8$ from PDF 38-1371, and is converged with R_p=7.27%, R_{wp}=10.4%, R_{exp}=7.06% and goodness-of-fit Chi^2=2.17 for the XRD data of sample x=0.04%. Comparison between the experimental and calculated results also confirms that the crystal phase of the sample belongs to the expected cubic non-centrosymmetric $P4_332$ (No. 212) space group.

The refinement shows that there is one type of Li site and two types of Ga and O sites. The refinement process produces lattice parameters of a=8.20349 Å and lattice volume V=552.073 $Å^3$ for sample with x=0.04% which are comparable to a=8.203 Å and V=551.970 $Å^3$ for the undoped $LiGa_5O_8$ sample. In order to determine the lattice sites occupancy for Cr^{3+}, the crystal structure of $LiGa_5O_8$ is also presented in Fig. 1(c). Each host cell unit consists of three basic units of [$Ga1O_6$] and [LiO_6] octahedra and [$Ga2O_4$] tetrahedra, respectively. Each Ga1-O1, Ga1-O2 and Li1-O2 bond has the same length of 2.05075 Å, and Ga1 and Li1 ions have the same coordination number of 6. Ga2 sites are 4-fold coordinated (CN=4), and the length of each Ga2-O2 bond is 1.77600 Å. Here, Cr^{3+} (r=0.615 Å, CN=6) may be preferable to substitute for $Ga1^{3+}$ (r=0.62 Å, CN=6) than Li^+ (r=0.76 Å, CN=6) ions considering the good match in ionic radii and respective valences.[40]

SEM image (upside in Fig.1 (d)) reveals the irregular columnar shape particles with an average size around 2 μm. The EDS spectrum (downside in Fig. 1(d)) confirms the existence of Ga, O and Cr elements, but no Li peaks can be detected because Li element cannot generate a reliable X-ray signal for detection.[41] Meanwhile, the unlabeled peaks came from Au element sputtered on the sample surface to improve conductivity for SEM measurements.

3.2 ML properties of $LiGa_5O_8:Cr^{3+}$

ML is observed in Cr^{3+} activated $LiGa_{5(1-x)}O_8:5xCr^{3+}$ phosphors. The ML band centered at ~716 nm is due to the $^2E \rightarrow {}^4A_2$ spin forbidden transition of Cr^{3+} in a 6-fold coordinated site.[42] First of all, we could analyze the ML spectra of Cr^{3+} doped samples in Fig. 2(a). When the x is 0.04%, the ML signal is too small to be recorded. The ML intensity gradually increases with the concentrations increase till x=0.12%, and then decreases with the further increase in Cr^{3+} content, confirming that the strongest ML intensity is for x=0.12%. Afterwards, in Fig. 2(b), the ML intensity dependence of sample x=0.12% versus various loading was studied and the related ML spectra are shown. With the increase in load value from 1000 to 3500 N, ML intensities continuously increases, demonstrating a linear correlation between the ML intensity and the load with a linear fitting R^2=0.9949 as seen Fig. 2(c), which makes the $LiGa_5O_8:Cr^{3+}$ phosphor suitable as stress sensor.

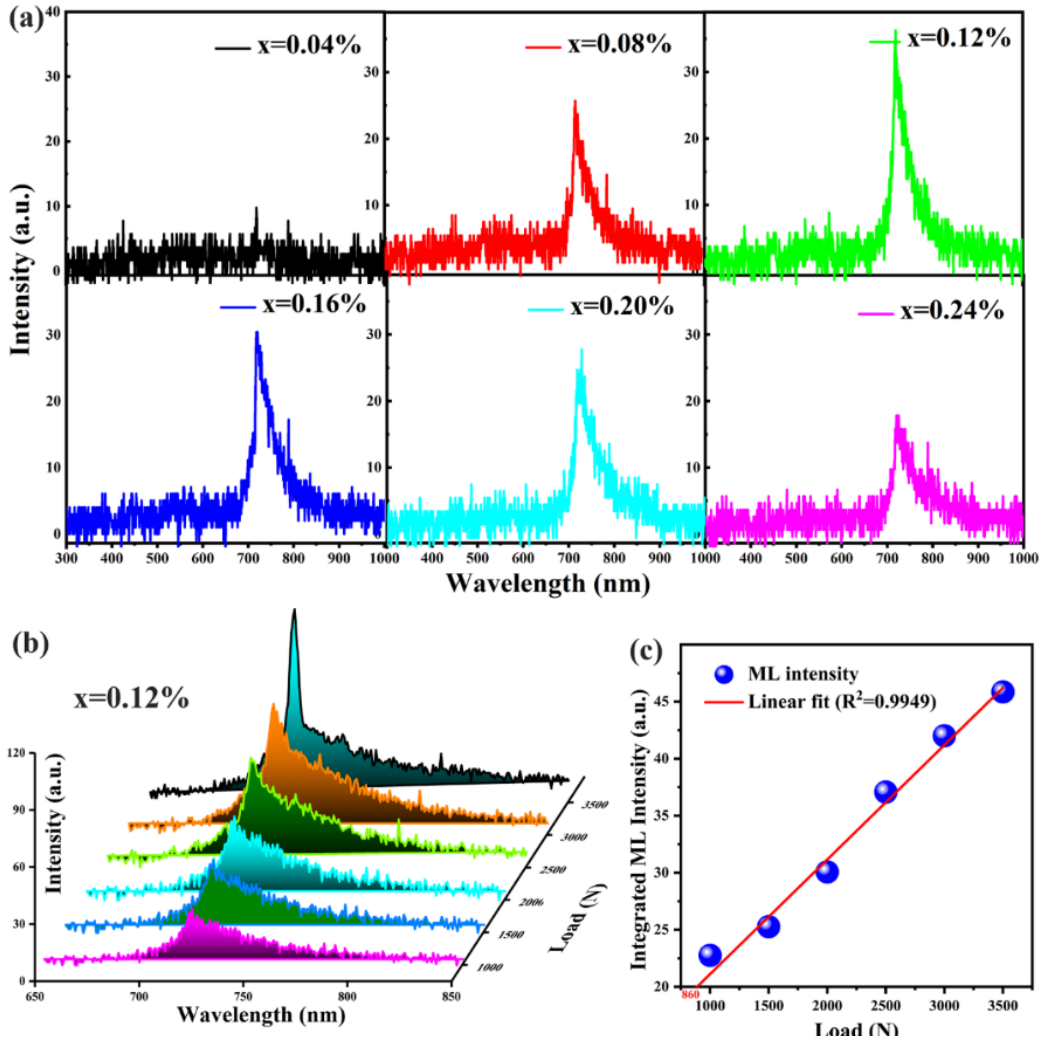

Fig. 2 ML features of $LiGa_{5(1-x)}O_8:5xCr^{3+}$. (a) ML spectra of $LiGa_{5(1-x)}O_8:5xCr^{3+}$ as a function of Cr^{3+} content (x=0.04%, 0.08%, 0.12%, 0.16%, 0.20% and 0.24%) under 1000 N load. (b) ML spectra of sample x=0.12% as a function of load (1000, 1500, 2000, 2500, 3000 to 3500 N. (c) Integrated ML intensity for spectra presented in (b). Notice that intercept is 860 N. Integrating range: 600-1000 nm.

3.3 Diffuse reflectance, PL, PLE and PersL properties of $LiGa_5O_8:Cr^{3+}$

To study the absorption/reflection performance of Cr^{3+} doped $LiGa_{5(1-x)}O_8:5xCr^{3+}$, the diffuse reflectance (DR) spectra of the samples are presented in Fig. 3(a). For each Cr^{3+} doped sample, DR spectrum shows a plateau in the wavelength range above 700 nm and a steep decrease with shoulders from 320 to 230 nm. The absorption near 230 nm could be attributed to the host band to band absorption, while other absorption bands centered at ~ 290, 420 and 590 nm correspond to the $^4A_2 \rightarrow {}^4T_1\,(^4P)$, $^4A_2 \rightarrow {}^4T_1\,(^4F)$ and $^4A_2 \rightarrow {}^4T_2\,(^4F)$ transitions of Cr^{3+} cations respectively. All of these absorption intensities are further enhanced with the increase

of Cr^{3+} content.[43] To experimentally estimate the bandgap energy, the plot of $[F(R\infty)h\nu]^2$ versus $(h\nu-E_g)$ is drawn in Fig. 3(b). $F(R\infty)$ originated from the Kubelka-Munk function: $F(R\infty)=(1-R\infty)^2/(2R\infty)$, wherein $R\infty$ is the reflectivity value, $h\nu$ is the photon energy and E_g is the optical bandgap energy. The spectrum demonstrates a linear dependence of $[F(R\infty)h\nu]^2$ to $(h\nu-E_g)$, indicating that $LiGa_5O_8$ is a direct-bandgap material. The optical bandgap energy of $LiGa_5O_8$ could be calculated as E_g=4.92 eV from the line extrapolation for $[F(R\infty)h\nu]^2$=0 (see Fig 3b).[44] Fig. 3(c-d) present the PL and PLE spectra of $LiGa_{5(1-x)}O_8$:5xCr^{3+} at room temperature. When monitoring the emission at 716 nm, the PLE spectra show several broad spectral bands ranging from 240 to 650 nm. The band peaking at 246 nm belongs to the host band to band absorption in good agreement with Fig. 3(a).[45] The band peaking at ~290 nm is due to the $^4A_2\rightarrow{}^4T_1$ (^4P) Cr^{3+} transition. Meanwhile, the two excitation bands centered at 418 nm and 600 nm resulted from the d-d intra-shell transitions of Cr^{3+} ions, which belong to the $^4A_2\rightarrow{}^4T_1$ (^4F) and $^4A_2\rightarrow{}^4T_2$ (^4F) transitions, respectively.[46, 47] We also measure the PL spectra of all Cr^{3+} doped samples between 650-830 nm under the 254 nm excitation, and one intense emission band centered at 716 nm can be observed in all samples, corresponding to the spin-forbidden $^2E\rightarrow{}^4A_2$ transition of Cr^{3+} in a 6-fold coordinated site.[48, 49] Meanwhile, the associated phonon side bands (PSB) are also observed in the PL spectra respectively at 726 and 738 nm for the Stokes PSB and at 701 nm for the anti-Stokes PSB.[45, 50] The inset of Fig. 3(d) shows the deep red colored image of sample x=0.12% under a 254 nm lamp. Meanwhile, an abnormal PL band is observed, as shown in the dotted red rectangle (730-830 nm), which results from the spin-allowed transition between the $^4T_2$ state and ground state of Cr^{3+}.[45] Moreover, from the spectral variation in Fig. 3(d), it can be speculated that the increase of Cr^{3+} doping concentration is beneficial to enhance the wide-band emission and inhibit the 716 nm emission. After being irradiated by a 254 nm UV lamp for 30 s, PersL spectra are detected and can be recorded, as shown in Fig. 3(e). Intriguingly, except for the PersL peak at 716 nm, another broad PersL band in the NIR range extending from 726 to 1000 nm can be observed. The PersL peak at 716 nm could be attributed to the $^2E\rightarrow{}^4A_2$ transition of Cr^{3+}, while the PersL broad band in the NIR range may originate from the spin-allowed transition $^4T_2\rightarrow{}^4A_2$ as already presented in the literature []. To figure out the dependence of the PL and PersL intensities at 716 nm and around 800 nm respectively versus Cr^{3+} content, the spectra in Fig.

3(f) combining figure 3 (d) and figure 3 (e) is reported.

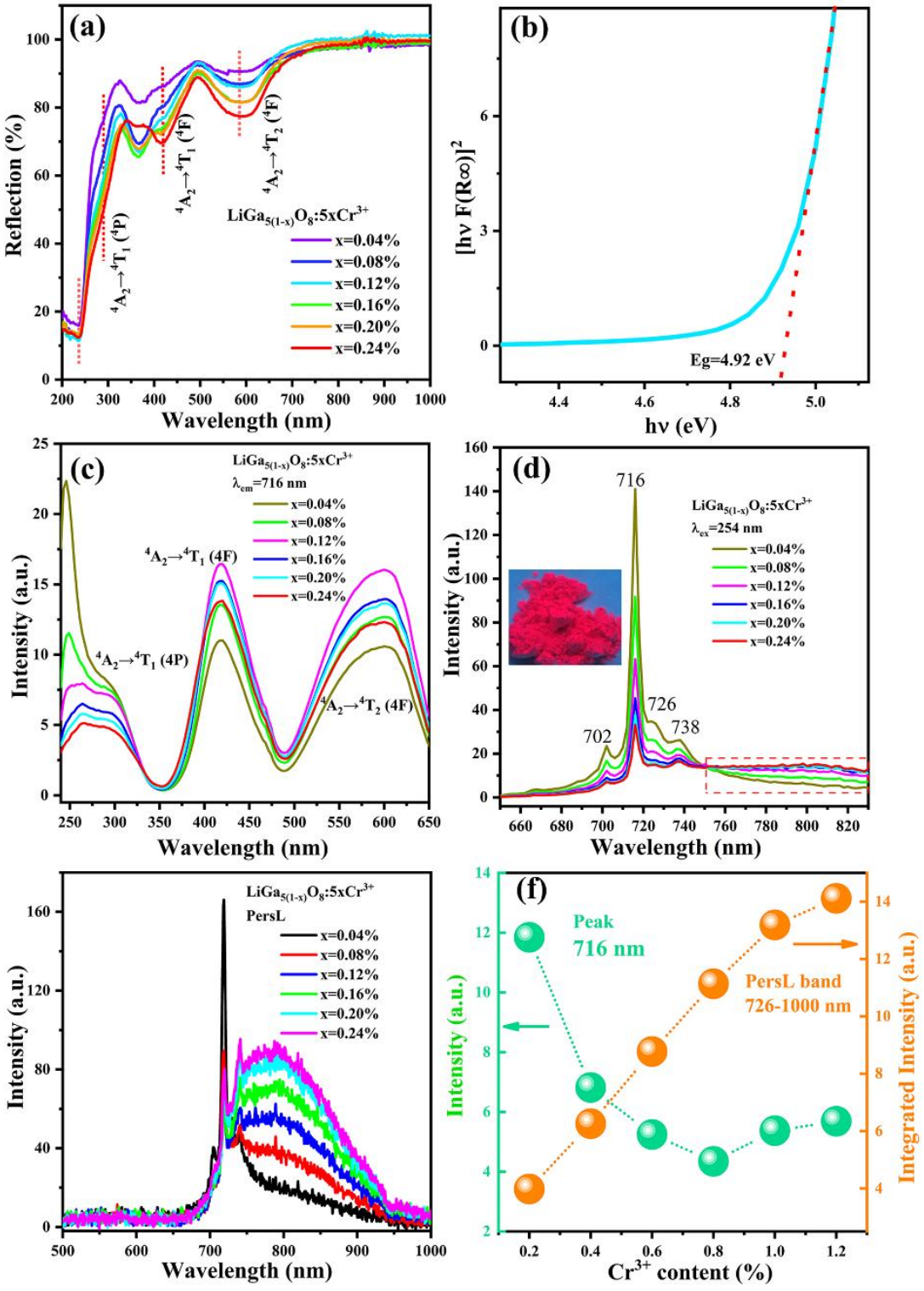

Fig. 3 Optical characteristics of $LiGa_{5(1-x)}O_8:5xCr^{3+}$. (a) DR spectra. (b) The plot of $[F(R\infty)h\nu]^2$ versus energy (eV). (c) PLE (λ_{em}=716 nm) and (d) PL (λ_{ex}=254 nm) spectra. The inset of (d) is the image of sample x=0.12% under a 254 nm lamp. (e) PersL spectra recorded after irradiated by a 254 nm lamp for 30 s. (f) The peak PersL intensities of 716 nm and the PersL band (726-1000 nm) as a function of Cr^{3+}

content. The composites are $LiGa_{5(1-x)}O_8:5xCr^{3+}$ (x=0.04%, 0.08%, 0.12%, 0.16%, 0.20% and 0.24%).

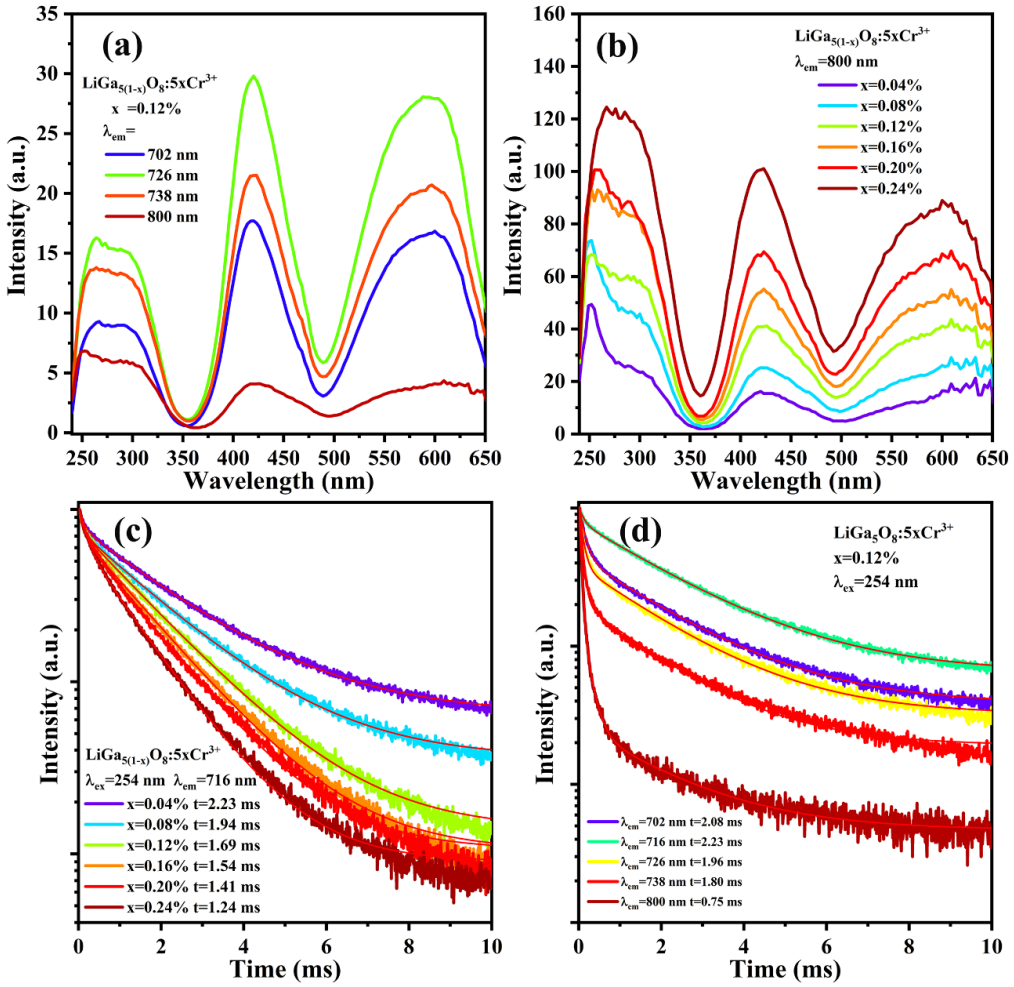

Fig. 4 Optical characteristics of $LiGa_{5(1-x)}O_8:5xCr^{3+}$. (a) PLE spectra of sample x=0.12% monitored at 702, 726, 738 and 800 nm. (b) PLE spectra of $LiGa_{5(1-x)}O_8:5xCr^{3+}$ monitored at 800 nm. The PL decay spectra of (c) $LiGa_{5(1-x)}O_8:5xCr^{3+}$ (x=0.04%, 0.08%, 0.12%, 0.16%, 0.20% and 0.24%) (λ_{ex}=254 nm, λ_{em}=716 nm), and (d) sample x=0.12% monitored under 254 nm excitation at the emission of 702, 716, 726, 738 and 800 nm, respectively.

With the increase in Cr^{3+} content, intensity of the 716 nm Cr^{3+}peak firstly decreases till x=0.16% and then increases with further increase of doping concentration. However, the PersL intensity of the band continuously increases even till x=0.24%, and this may indicate that higher Cr^{3+} doping concentration will result in enhanced transitions between $^4T_2$ state and ground state.[46] To further confirm the origin of the 702, 726, 738 nm PL peaks and the broad band PL (740-1000 nm), we measured the PLE and PL decay profile spectra as reported in Fig. 4. From these PLE spectra we first confirm that Cr^{3+} is the emitting center. Second,

emission at about 800 nm presents a slight red shift (see Fig. 4(a)) as already reported for a $^4T_2 \rightarrow {}^4A_2$ transition while both emissions at 702 nm and 726 nm may be attributed to $^2E \rightarrow {}^4A_2$ PSB emissions or Cr^{3+}/Cr^{3+} pairs that may affect the crystal field splitting [51, 52]. Furthermore, we also notice as expected that the PLE intensity at about 800 nm gradually increase with Cr^{3+} content (Fig. 4(b)) then a small band shift in the PLE spectra with Cr^{3+} content is noticeable (Fig. 4(a-b)), in regards to the R line emission at 716 nm. The lifetime values at various wavelengths, namely 702, 716, 726, 738 and 800 nm (of sample containing x=0.12%) can be determined based on equation: $\tau = \int I(t)t\mathrm{d}t / \int I(t)\mathrm{d}t$, where $I(t)$ represents the PL intensity at time t.[47] Obviously, ^2E unperturbed emission (716 nm) has the longest lifetime of 2.23 ms, and shorter lifetime (1.80 ms) is obtained for Cr-pairs (738 nm) in regard to the 716 nm one, while the shortest lifetime value (0.75 ms) corresponds to the spin allowed $^4T_2$ emission (800 nm) (Fig. 4(c-d)). Notice that the indicated values correspond to a thermal equilibrium between the ^2E and $^4T_2$ levels as expected for intermediate crystal field strength of Cr^{3+} cations in the $LiGa_5O_8$ host.

3.4 Insights in traps responsible for ML

In general, performances of both PersL and ML are closely related to traps.[53-56] TL measurement is extensively adopted to study the traps and thus could be employed here. Since there is no need for pre-irradiation of $LiGa_5O_8:Cr^{3+}$ to realize ML, one measure the TL glow curves of $LiGa_{5(1-x)}O_8:5xCr^{3+}$ (x=0, 0.04%, 0.08%, 0.12%, 0.16%, 0.20% and 0.24%) without first pre-irradiation process, as shown in Fig. 5(a). However, only negligible TL signals can be recorded in both $LiGa_5O_8$ hosts for various Cr^{3+} doped samples as seen Fig. 5(a), making very difficult the study of ML intensity dependence on traps. Notice that blackbody emission is observed for the higher temperatures (>500 K) in Fig. 5(a) and (d). Therefore, one measure the TL glow curves of $LiGa_5O_8$ and Cr^{3+} doped $LiGa_5O_8$ after pre-irradiation (Fig. 5(b)). These curves can be divided into three temperature ranges centered at ~390 K (P_1), 460 K (P_2) and 530 K (P_3), respectively. Based on Urbach empirical formula[57]: $E_T = T_m/500 = 23kT_m$, wherein E_T (eV) is the average trap depth and T_m (K) is peak temperature in TL glow curve, these traps are mainly located at the energy depth of 0.78 eV, and between 0.92 eV and 1.06 eV, respectively. Here, the suitable trap depths for PersL are widely recognized as 0.6-0.9 eV,[58, 59]

so we could proposed that deeper traps at about 1.06 eV may play special role in the ML properties of Cr^{3+} doped $LiGa_5O_8$. Furthermore, with the increase of Cr^{3+} content, the TL intensities of P_1 and P_2 firstly decrease to a minimum for x=0.12%, and then gradually increase. However, the trend is different for P_3.

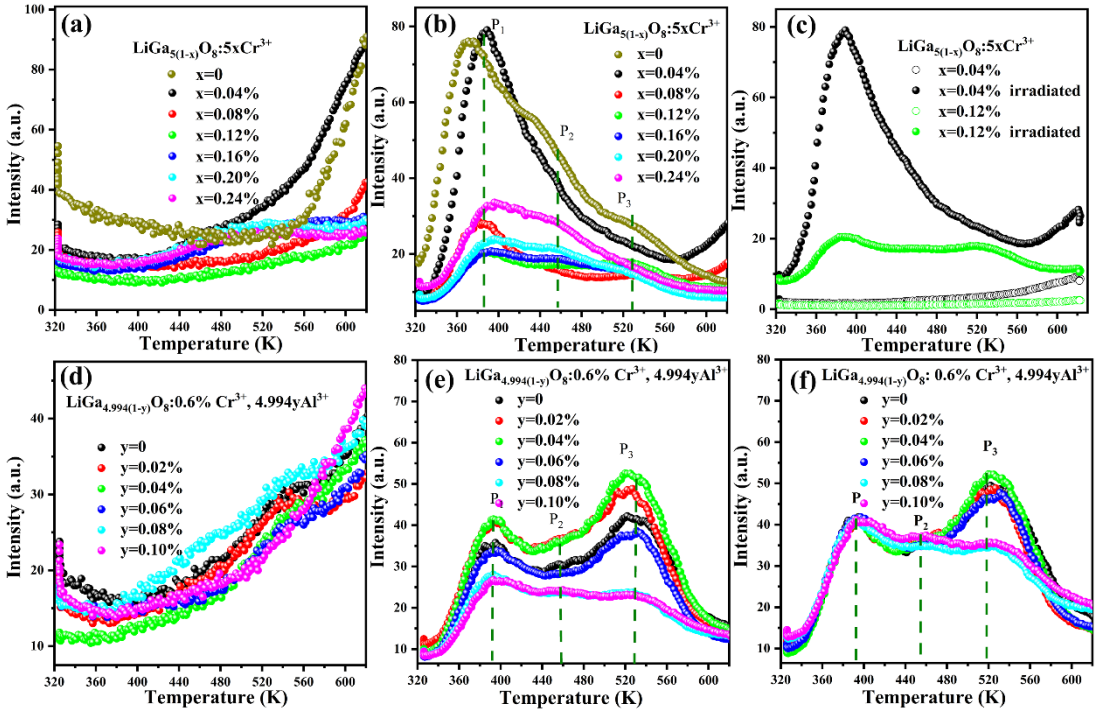

Fig. 5 Thermoluminescence glow curves and blackbody emission characteristics. (a) and (d) show the blackbody emissions of $LiGa_{5(1-x)}O_8:5xCr^{3+}$ and $LiGa_{4.994(1-y)}O_8:0.6\%Cr^{3+}$, $4.994yAl^{3+}$, respectively. (b) TL glow curves of $LiGa_{5(1-x)}O_8:5xCr^{3+}$ (x=0, 0.04%, 0.08%, 0.12%, 0.16%, 0.20% and 0.24%) over 320-620 K pre-irradiated by a 254 nm lamp for 30 s. (c) TL glow curves of samples x=0.04% and 0.12% before and after irradiated by a 254 nm lamp for 30 s. (e) TL glow curves of $LiGa_{4.994(1-y)}O_8:0.6\%Cr^{3+}$, $4.994yAl^{3+}$ (y= 0, 0.02%, 0.04%, 0.06%, 0.08% and 0.10%) over 320-620 K pre-irradiated by a 254 nm lamp for 30 s. (f) Normalized TL glow curves of (e) by the TL peak intensity at 390 K.

By comparing the TL glow curves of samples (x=0.04% and x=0.12%) before and after pre-irradiation by the 254 nm lamp (Fig. 5(c)), together with the fact that the x=0.12% sample shows stronger ML intensity than the x=0.04% sample and pre-irradiated samples present stronger ML intensity, one can guess that traps existing in P_3 play the more important in ML

process. Based on theses TL results and published data, traps may be defects formed during high-temperature sintering in air.[60]

Since traps corresponding to P_3 are the key factor for generating ML, a trap regulation or in others words a control of the trap distribution reducing the ratio of $(P_1+P_2)/P_3$ should be helpful to obtain stronger ML intensity. Following this idea, with taken as reference the best obtained ML sample ($LiGa_{4.994}O_8$:0.6%Cr^{3+}), we have prepared a series of ML phosphors by codoping with Al^{3+} ions in order to vary the trap distribution (namely $LiGa_{4.994(1-y)}O_8$:0.006Cr^{3+}, 4.994yAl^{3+}, y=0, 0.02%, 0.04%, 0.06%, 0.08% and 0.10%). TL glow curves of Cr^{3+}/Al^{3+} codoped samples after pre-irradiation were recorded, as shown in Fig. 5(e). Obviously, with the increase in Al^{3+} content from y=0 to 0.10%, the TL intensity of the phosphors firstly increases to a maximum at y=0.04%, and then decreases with further increase of doping concentration. In Fig. 5(f), we normalized the glow curves by the peak at 390 K and find that the ratio of $(P_1+P_2)/P_3$ is obviously the smallest at y=0.04%. Afterwards, we notice that these Al^{3+} codoped samples also reach a maximum value of the ML intensity at y=0.04% ($LiGa_{4.992}O_8$:0.6%Cr^{3+}, 0.2%Al^{3+}) (y=0.04%) (Fig. 6(a-b)). Of course single phases of the Al^{3+} codoped samples also have been confirmed as presented in Fig. 6(c). Thus, we confirm that traps located in P_3 thermal range efficiently contribute to ML. This is indeed quite important to increase the deep trap number for ML as the shallow traps and traps around 0.6-0.8 eV could be more rapidly emptied with temperature. Deeper traps (>0.9 eV) can only be emptied by ML or photostimulation. Following these discussions, bandgap engineering will provide a novel way to regulate ML through increasing deeper traps related to ML in regard to others traps. Thanks to Al-doping larger bandgap energy can be obtained favoring P3 glow curve.

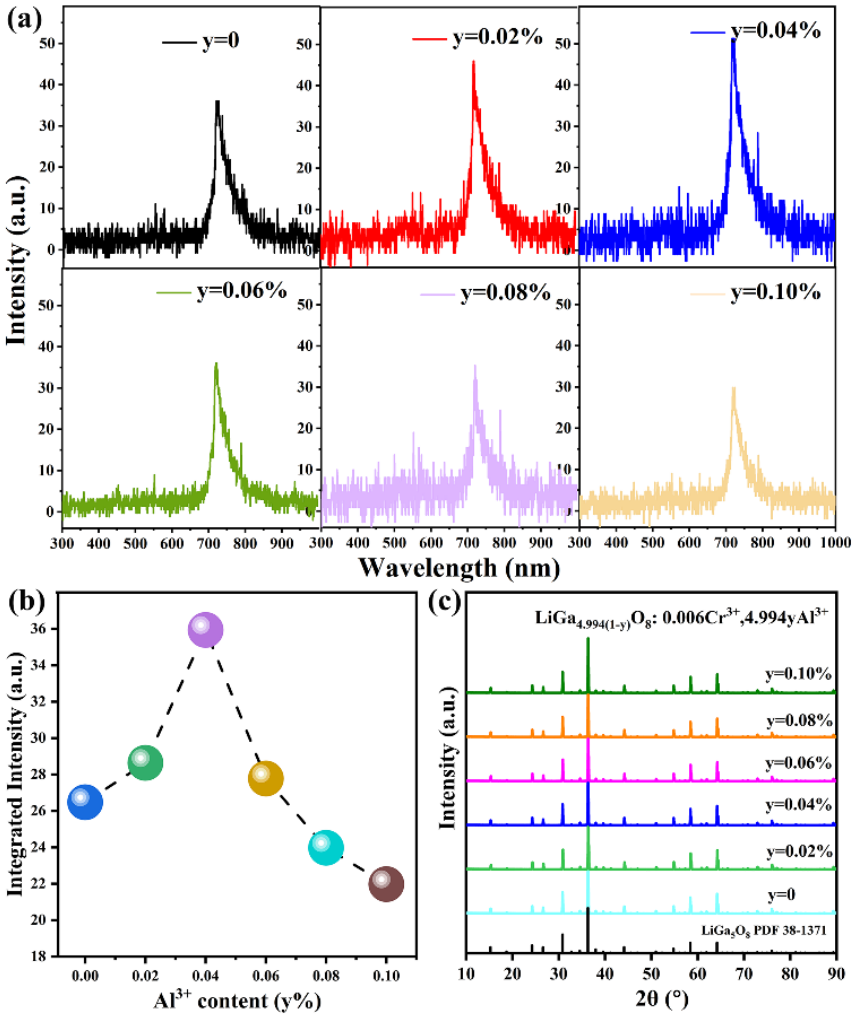

Fig. 6 ML and XRD spectra of $LiGa_{4.994(1-y)}O_8$:0.6%Cr^{3+}, 4.994yAl^{3+} (y=0, 0.02%, 0.04%, 0.06%, 0.08 and 0.10%). (a) ML spectra of different Al^{3+} codoped samples under the load of 1000 N. (b) Integrated ML intensities as a function of Al^{3+} content. Integrating range: 600-1000 nm. (c) XRD spectra of different Al^{3+} codoped samples and standard file of $LiGa_5O_8$ (PDF 38-1371).

3.5 Self-recoverability of ML and Mechanism for ML of $LiGa_5O_8:Cr^{3+}$

Since one can obtain ML signal without any light pre-irradiation process, it could be expected that this ML emission is self-recoverable. First of all, we recorded the ML spectra of $LiGa_{4.992}O_8$:0.6%Cr^{3+}, 0.2%Al^{3+} under 10 continuous load cycles as presented in Fig. 7. Each load cycle is designed to load 2000 N with 5 s of holding time before de-loading. ML in this system appears relatively self-recoverable in a dark room after each loading cycle, making the $LiGa_{4.992}O_8$:0.6%Cr^{3+}, 0.2%Al^{3+} compound highly promising as high-performance stress sensing materials.

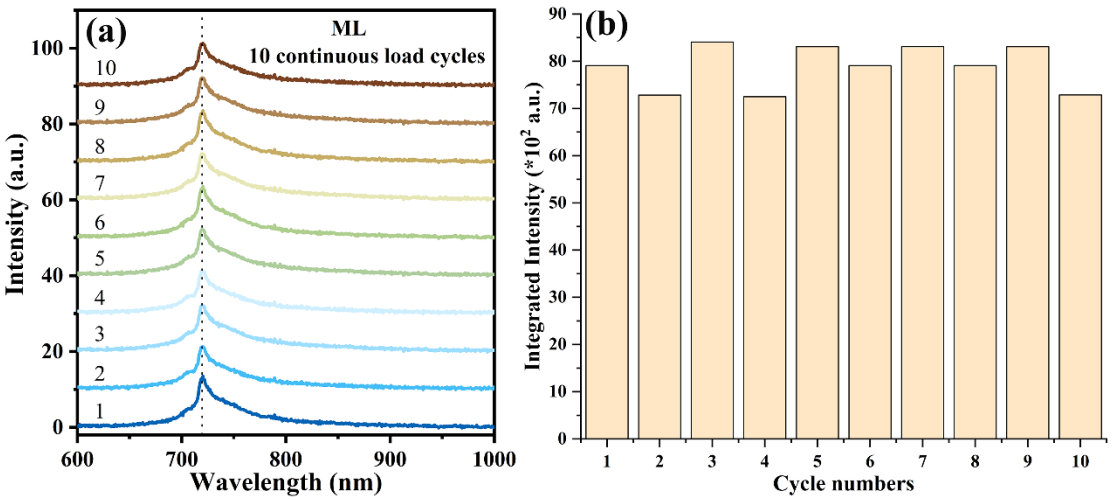

Fig. 7 (a) Self-recoverable ML spectra of $LiGa_{4.992}O_8$:0.6%Cr^{3+}, 0.2%Al^{3+}. Load cycle: 2000 N, holding time 5 s. (b) Integrated ML intensities over 600-1000 nm.

To further unravel the ML performances of the Cr-doped $LiGa_5O_8$, the density functional theory (DFT) has been applied to investigate the electronic structures. For the pristine $LiGa_5O_8$, the real spatial 3D orbital contour plot demonstrates that the active bonding and anti-bonding near the Fermi level (EF) are located near the O sites and Ga sites, respectively. The lattice displays an uniform electronic distribution (Fig. 8(a)). For the electronic structures, the projected partial density (PDOSs) of states are illustrated. Notably, the O-2p orbitals dominate the valence band maximum (VBM) while the s, p orbitals of Ga contribute to the conduction band minimum (CBM). The s-orbitals contribution of Li is very limited (Fig. 8(b)). With the introduction of the Cr into the lattice, the lattice structure has not been significantly affected, which is consistent with the experiment characterizations. However, we notice that the introduction of Cr leads to the uneven electronic distribution to form the local piezo electrical field in enhancing the charge separation and recombination. It is noted that the Cr-3d orbitals are playing a key role in both anti-bonding and bonding near EF (Fig. 8(c)). The PDOSs of Cr-doped $LiGa_5O_8$ further support the significant contribution of Cr in modifying the local electronic structures. Moreover, inter-electronic-levels are formed due to the Cr dopants, which facilitate the electron transfer to enhance the ML performances (Fig. 8(d)). To summarize the electron transfer behaviors, we have illustrated the gap states as the trap levels to actualize the ML. With the facilitation of the inter-electronic-levels, the large barriers for the electronic excitation and transition from the valence band (VB) to the

conduction band (CB) have been evidentially alleviated.

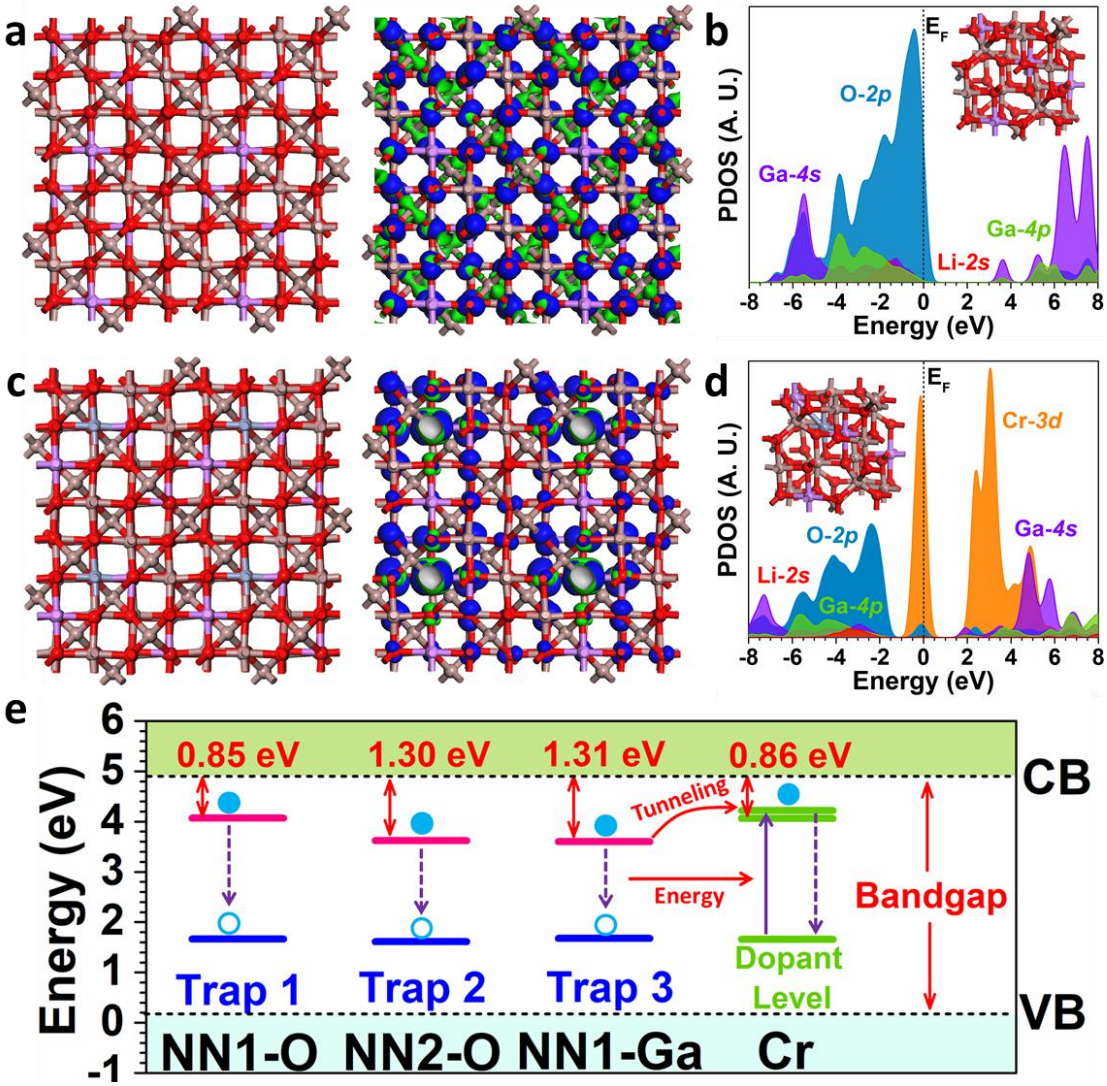

Fig. 8 (a) The lattice structure and real spatial 3D orbital contour plots for $LiGa_5O_8$. Purple balls= Li; Brown balls= Ga and Red balls= O. (b) The PDOSs of $LiGa_5O_8$. Inset: lattice structure of $LiGa_5O_8$. (c) The lattice structure and real spatial 3D orbital contour plots for Cr-doped $LiGa_5O_8$. Purple balls= Li; Brown balls= Ga; Red balls= O and Grey balls= Cr. (d) The PDOSs of Cr-doped $LiGa_5O_8$. Inset: lattice structure of Cr-doped $LiGa_5O_8$. (e) The summarized trap levels and electron transfer pathways for Cr-doped $LiGa_5O_8$.

The identified trap depths vary from 0.85 to 1.30 eV, which are close to the experimental observations, supporting the enhanced ML performance. Moreover, the dopant Cr display electronic levels close to the trap levels, which indicates two possible electron transfer channels to realize the ML. The electrons stored in the traps recombine with the hole to

supply energy for the excitation of Cr ions for luminescence. On the other hand, the electrons within the traps are also able to transfer energy to the excitation levels of Cr ions through tunneling due to the close energy levels, which further increases the ML efficiency (Fig. 8(e)). Therefore, the remarkable ML performances in Cr-doped $LiGa_5O_8$ is attributed to the formation of the local piezoelectric field by the perturbation to the electronic distribution as well as the induced traps states and appropriate inter-electronic-levels to promote the electron transfer and energy conversion.

3.6 Potential applications and outlooks

Being free of light charging process, this self-recoverable ML can be applied for in situ and real-time stress monitoring. Moreover, Cr^{3+} doped phosphors have been widely reported to show potential applications in bioimaging.[61] Thus, the ML of Cr^{3+} doped $LiGa_5O_8$ locating in the deep red to near infrared range (well adapted to the first biological window) is promising for biomechanical applications. As shown in Fig. 10, the ML light can be detected after passing through a piece of pork with 2 mm thickness at all the parts of skin, fat and lean (Fig. 9(d) shows the pork used in this experiment). Therefore, the Cr^{3+} doped $LiGa_5O_8$ phosphor can be potentially promising for bio-applications. As the ML here is self-recoverable, namely, we do not need any light pre-irradiation to power the phosphor during the whole operation process, therefore, we can reduce the potential irradiation induced damage to biological tissues. Although such ML is weak, our findings as presented here may shed light on in situ and real-time detection of intracorporal stress/strain.

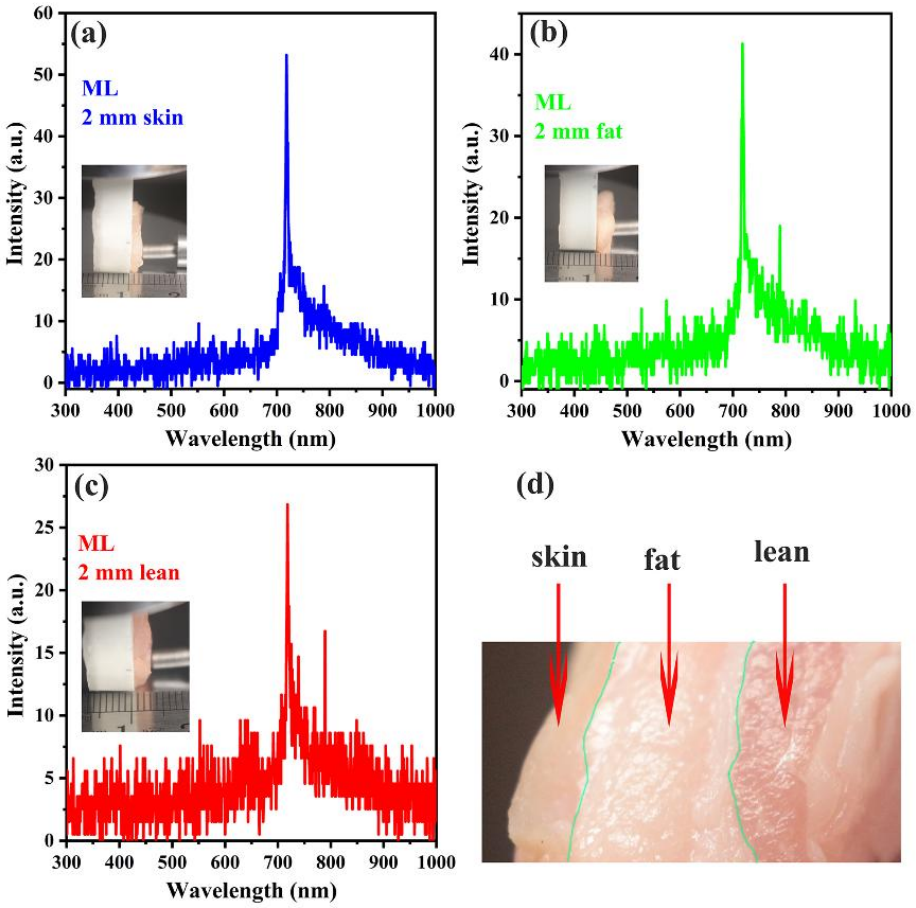

Fig. 9 ML spectra after passing through 2 mm thick pork at the part of (a) skin, (b) fat and (c) lean. (d) Digital-camera photo of the pork used in this experimental.

Further study can be focused on the following two aspects: i) Although we have presented a way to increase ML intensity by increasing the ratio of deeper traps through codoping with Al^{3+} ions and enlarging the bandgap, such a regulation is limited and methods for further intensity enhancement should be explored. ii) Regarding the deep red wavelength of ML peaking at 716 nm, developing new ML phosphors at longer wavelength in the first biological window and near infrared range suitable for deep in vivo applications is of great importance. Of course the next step will also be the preparation of nanosize, stable and dispersible materials keeping the properties at the highest level.

4 Conclusions

In summary, for the first time, we report the self-recoverable ML behavior in $LiGa_5O_8:Cr^{3+}$. The ML of $LiGa_5O_8:Cr^{3+}$ is located in the deep red wavelength range, where there is no

efficient ML material. In contrast to most ML materials which require light pre-irradiation to power ML emission, ML from $LiGa_5O_8:Cr^{3+}$ phosphor can be triggered solely by mechanical loading. The present work compared PersL, TML, ML and PL, and the relationship between ML intensity and TL performance. In that sense, we demonstrated that the traps responsible for ML are localized deeper in energy than 1 eV. Consequently, Al^{3+} ions are introduced in the host in replacement of Ga to regulate the trap distribution and the bandgap for optimizing the ML performance. Efficient ML is achieved in $LiGa_{4.992}O_8$:0.6%Cr^{3+}, 0.2%Al^{3+} sample. We have demonstrated that the ML of $LiGa_5O_8:Cr^{3+}$ is self-recoverable without pre-irradiation light after every mechanical loading cycle. A possible mechanism is proposed to elucidate the self-recoverable ML of $LiGa_5O_8:Cr^{3+}$. DFT calculations confirm that Cr dopants leads to the alleviation of electron excitation barriers from CB to VB through the formation of states into the bandgap, which prolong of ML through shallow electron traps and improved electronic transfer. The present work not only enriches the candidates for ML materials, but also may help us build more comprehensive understandings toward the mechanism of ML. Finally, we have demonstrated that the ML light can penetrate in 2 mm-thick pork at all parts including skin, fat and lean. This is very promising for using $LiGa_5O_8:Cr^{3+}$ phosphor for further *in vivo* event if there is still a long path toward these applications.

Conflicts of interest

There are no conflicts to declare.

Acknowledgements

We acknowledge financial support from National Natural Science Foundation of China (Grant No. 51672085, 51872095), Program for Innovative Research Team in University of Ministry of Education of China (Grant No. IRT_17R38), Major Basic Research Cultivation Project of Natural Science Foundation of Guangdong Province (Grant No.2018B03038009), Local Innovative Research Team Project of "Pearl River Talent Plan" (Grant No. 2017BT01X137). P. X. Xiong thank Z. Q. Huang for his help with the SEM test, H. Y. Luo for his help with the discussions on DR experiment, R. H. Ma for his help in the ML test.

References

1. R. R. Petit, S. E. Michels, A. Feng and P. F. Smet, Light Sci Appl 8 (2019) 124.
2. X. Wang, D. Peng, B. Huang, C. Pan and Z. L. Wang, Nano Energy 55 (2019) 389-400.
3. J.-C. Zhang, X. Wang, G. Marriott and C.-N. Xu, Pro Mater Sci 103 (2019) 678-742.
4. C. Chen, Y. Zhuang, D. Tu, X. Wang, C. Pan and R.-J. Xie, Nano Energy 68 (2020) 104329.
5. A. Feng, S. Michels, A. Lamberti, W. Van Paepegem and P. F. Smet, Acta Mater 183 (2020) 493-503.
6. F. Wang, F. Wang, X. Wang, S. Wang, J. Jiang, Q. Liu, X. Hao, L. Han, J. Wang, C. Pan, H. Liu and Y. Sang, Nano Energy 63 (2019) 103861.
7. L. Liu, C.-N. Xu, A. Yoshida, D. Tu, N. Ueno and S. Kainuma, Adv Mater Tech 2018, DOI: 10.1002/admt.201800336, 1800336.
8. M. C. Wong, L. Chen, G. Bai, L. B. Huang and J. Hao, Adv Mater 29 (2017) 129.
9. X. Y. Wei, X. Wang, S. Y. Kuang, L. Su, H. Y. Li, Y. Wang, C. Pan, Z. L. Wang and G. Zhu, Adv mater 28 (2016) 6656.
10. X. Wang, H. Zhang, R. Yu, L. Dong, D. Peng, A. Zhang, Y. Zhang, H. Liu, C. Pan and Z. L. Wang, Adv mater 27 (2015) 2324.
11. W. Li, Q. Huang, Z. Mao, Q. Li, L. Jiang, Z. Xie, R. Xu, Z. Yang, J. Zhao, T. Yu, Y. Zhang, M. P. Aldred and Z. Chi, Angew Chem Int Ed 2018, DOI: 10.1002/anie.201806861.
12. R. S. Fontenot, K. N. Bhat, W. A. Hollerman and M. D. Aggarwal, Materials Today 14 (2011) 292-293.
13. A. Incel, M. Emirdag-Eanes, C. D. McMillen and M. M. Demir, ACS Appl Mater Interfaces 9 (2017) 6488-6496.
14. Q. Hua, J. Sun, H. Liu, R. Bao, R. Yu, J. Zhai, C. Pan and Z. L. Wang, Nat Commun 9 (2018) 244.
15. L. Li, L. Wondraczek, M. Peng, Z. Ma and B. Zou, Nano Energy 69 (2020) 104413.
16. X. Zhang, J. Zhao, B. Chen, T. Sun, R. Ma, Y. Wang, H. Zhu, D. Peng and F. Wang,

Adv Opt Mater 2020, DOI: 10.1002/adom.202000274.

17. D. Peng, Y. Jiang, B. Huang, Y. Du, J. Zhao, X. Zhang, R. Ma, S. Golovynskyi, B. Chen and F. Wang, Adv Mater 32 (2020) 1907747.
18. P. Xiong and M. Peng, J Mater Chem C 7 (2019) 6301-6307.
19. H. Zhang, D. Peng, W. Wang, L. Dong and C. Pan, The J Phy Chem C 119 (2015) 28136-28142.
20. H. Li, Y. Zhang, H. Dai, W. Tong, Y. Zhou, J. Zhao and Q. An, Nanoscale 10 (2018) 5489-5495.
21. P. Xiong, M. Peng, J. Cao and X. Li, J Am Cera Soc 102 (2019) 5899-5909.
22. B. Huang, M. Sun and D. Peng, Nano Energy 47 (2018) 150.
23. S. M. Jeong, S. Song, S. K. Lee and N. Y. Ha, Adv mater 25 (2013) 6194.
24. K.-S. Sohn, S. Timilsina, S. P. Singh, T. Choi and J. S. Kim, APL Mater 4 (2016) 106102.
25. J. Botterman, K. V. d. Eeckhout, I. D. Baere, D. Poelman and P. F. Smet, Acta Mater 60 (2012) 5494-5500.
26. Y. Du, Y. Jiang, T. Sun, J. Zhao, B. Huang, D. Peng and F. Wang, Adv mater 2018, DOI: 10.1002/adma.201807062, e1807062.
27. D. Tu, C. N. Xu, A. Yoshida, M. Fujihala, J. Hirotsu and X. G. Zheng, Adv mater 29 (2017) 129.
28. W. Wang, D. Peng, H. Zhang, X. Yang and C. Pan, Opt Commun 395 (2017) 24.
29. H. Chen, X. Sun, G. D. Wang, K. Nagata, Z. Hao, A. Wang, Z. Li, J. Xie and B. Shen, Mater Hori 4 (2017) 1092-1101.
30. F. Liu, W. Yan, Y. J. Chuang, Z. Zhen, J. Xie and Z. Pan, Sci Rep 3 (2013) 1554.
31. P. Xiong, M. Peng, K. Qin, F. Xu and X. Xu, Adv Opt Mater 7 (2019) 1901107.
32. S. J. Clark, M. D. Segall, C. J. Pickard, P. J. Hasnip, M. J. Probert, K. Refson and M. C. Payne, Zeitschrift Fur Kristallographie 220 (2005) 567-570.
33. S. J. Clark, M. D. Segall, C. J. Pickard, P. J. Hasnip, M. I. J. Probert, K. Refson and M. C. Payne, Zeitschrift für Kristallographie - Crystalline Materials 220 (2005) 1220.
34. J. P. Perdew, K. Burke and M. Ernzerhof, Phys Rev Lett 77 (1996) 3865-3868.
35. P. J. Hasnip and C. J. Pickard, Comput. Phys Commun 174 (2006) 24-29.

36. J. P. Perdew, J. A. Chevary, S. H. Vosko, K. A. Jackson, M. R. Pederson, D. J. Singh and C. Fiolhais, Physical Review B 46 (1992) 6671-6687.
37. D. Vanderbilt, Physical Review B 41 (1990) 7892-7895.
38. J. D. Head and M. C. Zerner, Chem Phys Lett 122 (1985) 264-270.
39. M. I. J. Probert and M. C. Payne, Physical Review B 67 (2003) 167.
40. W. Yang, J. Li, B. Liu, X. Zhang, C. Zhang, P. Niu and X. Jiang, Nanoscale 10 (2018) 19039.
41. J. L. Goldman, B. R. Long, A. A. Gewirth and R. G. Nuzzo, Adv Funct Mater 21 (2011) 2412-2422.
42. H. X. Zhao, C. X. Yang and X. P. Yan, Nanoscale 8 (2016) 18987.
43. X. Lin, R. Zhang, X. Tian, Y. Li, B. Du, J. Nie, Z. Li, L. Chen, J. Ren, J. Qiu and Y. Hu, Adv Opt Mater 6 (2018) 1701161.
44. H. Li, R. Pang, G. Liu, W. Sun, D. Li, L. Jiang, S. Zhang, C. Li, J. Feng and H. Zhang, Inorg Chem 57 (2018) 12303-12311.
45. O. Q. De Clercq and D. Poelman, ECS Journal of Solid State Science and Technology 7 (2018) 3171-3175.
46. O. Q. De Clercq, J. Du, P. F. Smet, J. J. Joos and D. Poelman, Phys Chem Chem Phys 20 (2018) 30455-30465.
47. B. Viana, S. K. Sharma, D. Gourier, T. Maldiney, E. Teston, D. Scherman and C. Richard, J Lumin 170 (2016) 879-887.
48. G. Liu, S. Zhang, Y. Shi, X. Huang, Y. Tang, P. Chen, W. Si, W. Huang and X. Dong, Adv Funct Mater 28 (2018) 1804317.
49. W. Fan, N. Lu, C. Xu, Y. Liu, J. Lin, S. Wang, Z. Shen, Z. Yang, J. Qu, T. Wang, S. Chen, P. Huang and X. Chen, ACS Nano, 11 (2017) 5864-5872.
50. D. Gourier, A. Bessière, S. K. Sharma, L. Binet, B. Viana, N. Basavaraju and K. R. Priolkar, Phy and Chem Sol 75 (2014) 826-837.
51. H. Lin, G. Bai, T. Yu, M.-K. Tsang, Q. Zhang and J. Hao, Adv Opt Mater 5 (2017) 1700227.
52. V. Đorđević, M. G. Brik, A. M. Srivastava, M. Medić, P. Vulić, E. Glais, B. Viana and M. D. Dramićanin, Opt Mate 74 (2017) 46-51.

53. P. Xiong and M. Peng, J Mater Chem C 7 (2019) 8303-8309.
54. Z. Pan, Y. Y. Lu and F. Liu, Nat Mater 11 (2011) 58-63.
55. P. Xiong and M. Peng, Opt Mater: X 2 (2019) 100022.
56. S. K. Sharma, D. Gourier, B. Viana, T. Maldiney, E. Teston, D. Scherman and C. Richard, Opt Mater 36 (2014) 1901-1906.
57. A. J. J. Bos, R. M. van Duijvenvoorde, E. van der Kolk, W. Drozdowski and P. Dorenbos, J Lumin 131 (2011) 1465-1471.
58. Y. Zhuang, L. Wang, Y. Lv, T.-L. Zhou and R.-J. Xie, Adv Funct Mater 28 (2018) 1705769.
59. J. Xu, D. Murata, J. Ueda, B. Viana and S. Tanabe, Inorg Chem 57 (2018) 5194-5203.
60. E. Finley and J. Brgoch, J Mater Chem C 7 (2019) 2005-2013.
61. Y. Li, M. Gecevicius and J. Qiu, Chem Soc Rev 45 (2016) 2090-2136.